11th World Congress on Computational Mechanics (WCCM XI)
5th European Conference on Computational Mechanics (ECCM V)
6th European Conference on Computational Fluid Dynamics (ECFD VI)
E. Oñate, J. Oliver and A. Huerta (Eds)

AN LES-LIKE STABILIZATION OF THE SPECTRAL ELEMENT SOLUTION OF THE EULER EQUATIONS FOR ATMOSPHERIC FLOWS

Simone Marras, Andreas Müller, Francis X. Giraldo

Naval Postgraduate School, Dept. of Applied Mathematics
833 Dyer Road, Bldg. 232, Spanagel 249A Monterey, CA 93943-5216 U.S.A.
smarras1@nps.edu; fxgirald@nps.edu

Key words: Spectral Element Method; Euler Equations; LES; Stabilization; Non-Hydrostatic Atmospheric Flow; Moist Dynamics; Squall Line Simulations

Abstract. The solution of the Euler equations by the spectral element method (SEM) is subject to oscillatory behavior if the high-frequency modes are not damped in some way. In this analysis, we extend to high order spectral elements and to low-Mach number flows the recent work by Nazarov and Hoffman [20], where an LES-like physical diffusion acts both as a localized and controlled numerical stabilization for finite elements and as a turbulence model for compressible flows. In the framework of high-order SEM for the solution of the low-Mach number flows, this approach is a possible physics-based alternative to the variational multiscale stabilization (VMS) method that the authors successfully applied to the SEM solution of the advection diffusion equation [17] in the context of atmospheric flows. Like for VMS, stabilization is obtained by means of a residual-based term that is added to the inviscid Euler equations. Unlike VMS, however, this extra term is based on purely physical –rather than numerical– assumptions, in that it is related to the viscous component of the stress tensor of the Navier-Stokes equations. The method is tested with pseudo and fully 3D simulations of idealized nonhydrostatic atmospheric flows and is verified against data from the literature. This work represents a step toward the implementation of a stabilized, high order, spectral element LES model within the *Nonhydrostatic Unified Model of the Atmosphere* (NUMA) developed by the authors.

1 Introduction

Recently, a numerically stable and computationally inexpensive large-eddy simulation (LES) model for compressible flows was designed for adaptive finite elements in [20]. In this work, we explore the capabilities of that LES model to act as a stabilization

method for the spectral element solution of the Euler equations at the low Mach number regimes typical of atmospheric flows. This effort is justified by the fact that, within the community of atmospheric modelers, there is still a widespread concern about the most proper stabilization scheme to be used with either Galerkin or other approximation methods of the equations of atmospheric dynamics. Although the use of residual-based stabilizing schemes has been largely assessed for the finite element method during the past thirty years (e.g. Streamline-Upwind/Petrov-Galerkin (SUPG) [2], Galerkin/Least-Squares (GLS) [10], Variational Multiscale (VMS) [9, 8, 18]), hyper viscosity is still today the most classical approach used by atmospheric modelers in spite of its important drawbacks (see, e.g. [11]). With this work, we propose a possible physics-based alternative to the VMS scheme that the authors successfully applied to the spectral element solution of the advection-diffusion equation in [17], and show its capabilities to produce accurate and stable solutions of 3D dry and moist atmospheric flows that are fully comparable with the literature. Although this is an LES model, however, much additional work is necessary to fully assess its applicability as a turbulence closure for atmospheric simulations, and is now left out of the scope of this paper. This effort is a first step that the authors are making toward the implementation of a stabilized high order spectral element LES model (LES-SEM) within the *Nonhydrostatic Unified Model of the Atmosphere* (NUMA) developed by the authors ([13, 6]).

The rest of the paper is organized as follows. The sets of equations and the LES model are described in Section 2. The numerical method of discretization of these equations is reported in Section 3, which is followed by the numerical tests and results in Section 4. The concluding remarks are given in Section 5.

2 Equations sets

We are interested in the solution of the Euler equations for dry and moist flows. The model is described in the following two subsections where the equations for dry dynamics, the LES model, and the prognostic equations of water quantities in the atmosphere are described.

2.1 Dry dynamics

Let $\Omega \in \mathbb{R}^3$ be a fix three dimensional domain with boundary $\partial\Omega$. Let us also define the set $\mathbf{q} = [\rho\ \mathbf{u}\ \theta]^{\mathcal{T}}$ of the unknown density, velocity, and potential temperature. $\mathcal{T}$ indicates the transpose operation. The strong form of the time-dependent Euler equations with gravity, g, is written as:

$$\begin{aligned} \rho_t + \mathbf{u}\cdot\nabla\rho + \rho\nabla\cdot\mathbf{u} &= 0 \\ \mathbf{u}_t + \mathbf{u}\cdot\nabla\mathbf{u} + \tfrac{1}{\rho}\nabla\cdot(\mathbf{I}p) &= g\mathbf{k} \\ \theta_t + \mathbf{u}\cdot\nabla\theta &= 0 \end{aligned} \tag{1}$$

where p is the pressure, $\mathbf{I}$ is the rank-3 identity tensor, and $\mathbf{k}$ is the unit vector $[0\,0\,1]^{\mathcal{T}}$. Equations (1) must be solved in $\Omega\ \forall t \in (0,T)$. It is understood that proper initial and boundary conditions must be assigned. This system of five equations and six unknowns is closed by the equation of state for a perfect gas

$$p = C_0(\rho\theta)^{\gamma}, \tag{2}$$

where $C_0 = R^{\gamma}/p_0^{\gamma-1}$. $R = 287\,\mathrm{Jkg^{-1}K^{-1}}$ is the gas constant dry air, γ is the ratio of the coefficients of specific heat at constant pressure, c_p, and volume, c_v, and p_0 is a reference pressure that we take equal to $1000\,hPa$. Using the equation of state, we express the space derivative of pressure, ∇p, as a function of ρ and θ and write:

$$\nabla p = C_0\nabla(\rho\theta)^{\gamma} = C_0\gamma(\rho\theta)^{\gamma-1}\left[\rho\nabla\theta + \theta\nabla\rho\right].$$

2.2 LES-like stabilization

The straightforward approximation of (1) by spectral elements is known to lose numerical stability, with Gibbs oscillations that cause the solution to lose its accuracy. As a way to stabilize the problem, the Euler equations are corrected to include a residual-based viscosity in the way described below. The viscous terms are added to the right-hand side of the Equations (1). We write:

$$\begin{aligned} \rho_t + \mathbf{u}\cdot\nabla\rho + \rho\nabla\cdot\mathbf{u} &= \nabla\cdot(\nu_n\nabla\rho) \\ \mathbf{u}_t + \mathbf{u}\cdot\nabla\mathbf{u} + \tfrac{1}{\rho}\nabla\cdot(\mathbf{I}p) &= \tfrac{1}{\rho}\nabla\cdot\left(\mu_n\left(\nabla\mathbf{u} + \nabla\mathbf{u}^{\mathrm{T}}\right)\right) + g\mathbf{k} \\ \theta_t + \mathbf{u}\cdot\nabla\theta &= \nabla\cdot(\kappa_n\nabla\theta). \end{aligned} \tag{3}$$

The new viscosity coefficient that appear in Equations (3) are computed dynamically as a function of the solution. They are calculated element-wise on every high order element K. More specifically, given the sensible temperature $T = \theta(p/p_0)^{R/c_p}$ and one element with linear equivalent length $\bar{h}_K$, we start by defining the dynamic viscosities

$$\mu_{\max}|_K = 0.5\bar{h}_K\,\|\rho^n\|_{\infty,K}\,\||\mathbf{u}^n| + \sqrt{c_pT^n}\|_{\infty,K}, \tag{4}$$

and

$$\mu_1|_K = \bar{h}_K^2 \, \|\rho^n\|_{\infty,\Omega} \max\left(\frac{\|R(\rho)\|_{\infty,K}}{\|\rho^n\|_{\infty,\Omega}}, \frac{\|R(\mathbf{u})\|_{\infty,K}}{\|\mathbf{u}^n - \bar{\mathbf{u}}^n\|_{\infty,\Omega}}, \frac{\|R(\theta)\|_{\infty,K}}{\|\theta^n - \bar{\theta}^n\|_{\infty,\Omega}} \right), \tag{5}$$

where $\bar{\cdot}$ indicates the space average of the quantity at hand over Ω and the $\|\cdot\|_{\infty,\Omega}$ terms at the denominator are used for normalization for a consistent dimension of the resulting equation. Having $\mu_{\max}$ and μ_1 constructed, we can compute the dynamics coefficients of the viscosity terms in Equations (3) as:

$$\mu_n|_K = \min\left(\mu_{\max}|_K, \mu_1|_K\right), \quad \kappa_n|_K = \frac{\Pr}{c_p - 1}\mu_n|_K, \quad \nu_n|_K = \frac{\Pr}{\|\rho^n\|_{\infty,K}}\mu_n|_K, \tag{6}$$

where $Pr = 0.1$ is an artificial Prandtl number suggested in [20]. In the case of atmospheric flows, we expect that the optimal Prandtl number may differ from the suggested value above. However, at the current stage of this work, we have not made any additional analysis to verify our statement.

2.3 Moist dynamics

When the atmosphere contains moisture, Equations (3) must be modified to include the effect of water tracers and must be coupled to a set of additional transport equations that model the dynamics of moisture. Given the scope of this paper, it will suffice for us to model the simplest of water interactions in the atmosphere: specifically, condensation of water vapor into clouds and formation of rain water and precipitation. For this purpose, the microphysical processes are modeled by means of the Kessler parameterization [14].

The water substances are treated in terms of the mixing ratio of water vapor, q_v, cloud water, q_c, and rain, q_r, that, given a mass per unit volume of dry air, ρ_d, are defined as

$$q_i = \frac{\rho_i}{\rho_d} \qquad i = v, c, r.$$

Because moist air contributes with a positive buoyancy to the momentum of the flow, the buoyancy term $B = g\mathbf{k}$ in the Euler equations above is corrected as follows:

$$B = g(1 + \epsilon q_v + q_c - q_r)\mathbf{k}, \tag{7}$$

where $\epsilon = R/R_v$ is the ratio of the gas constant of dry air and the gas constant $R_v = 461\text{Jkg}^{-1}\text{K}^{-1}$ of water vapor. Furthermore, due to the microphysical processes that involve phase changes in the water content, a source/sink term that includes the latent heat release or gain is added to the right-hand side of the equation of potential temperature: $S_\theta = f(L_v)$ (for details on this term, the reader is referred to [15]).

The mixing ratios q_v, q_c and q_r in Equation 7 are computed from the solution of the three additional advection-reaction equations

$$q_{i_t} + \mathbf{u} \cdot \nabla q_i \quad = \quad S_{q_i}(\rho, q_v, q_c, q_r) \qquad \forall\, i = v, c, r, \tag{8}$$

where $S_{q_i}(\rho, q_v, q_c, q_r)$ are the sources and sinks that are computed as a function of the microphysical processes in the Kessler scheme. The systems (3) and (8) are coupled and are solved in two steps through the classical saturation adjustment technique (see [23]).

3 Space and time discretization

3.1 Spectral element approximation

To solve (3) and (8) by the spectral element method on a domain Ω, we proceed by defining the weak form of the two systems that we first write in compact and general form as

$$\frac{\partial \mathbf{q}}{\partial t} + \mathcal{L}(\mathbf{q}) = \mathbf{S}(\mathbf{q}), \tag{9}$$

where $\mathcal{L}$ and $\mathbf{S}$ are the differential operator in space and the source terms that can be easily identified in the five + three equations above. Given a basis function ψ that belongs to the Sobolev space H^1, the weak form of (9) is given by the integral

$$\int_\Omega \psi \left[\frac{\partial \mathbf{q}}{\partial t} + \mathcal{L}(\mathbf{q}) - \mathbf{S}(\mathbf{q}) \right] d\Omega = 0. \tag{10}$$

The weak form of the diffusion operators is obtained, as usual, by integration by parts. The integrals above are solved element-wise on the discrete polyhedral approximation Ω^h of the domain Ω. The discrete domain Ω^h is defined by the union of N_e non-overlapping quadrilateral elements Ω_e^h. For every element we define a bijective transformation $\mathcal{F}_{\Omega_e^h} : (x, y, z) \to (\xi, \eta, \zeta)$ that maps the physical coordinate system, (x, y, z) to the reference system (ξ, η, ζ) where the reference element $\hat{\Omega}_e^h(\xi, \eta) = [-1, 1] \times [-1, 1] \times [-1, 1]$ lives. The Jacobian matrix of the transformation has components $J^i = \partial_\xi \mathcal{F}^i$ and determinant $|\mathbf{J}|$. Given the definition of the reference element, the element-wise solution can be approximated by the expansion

$$q_N(\mathbf{x}, t)|_{\Omega_e} = \sum_{k=1}^{(N+1)^3} \psi_k(\mathcal{F}_{\Omega_e}^{-1}(\mathbf{x}))\, q_N(\mathbf{x}_k, t),\ e = 1, \ldots, N_e \tag{11}$$

where $(N+1)^3$ is the number of collocation points within the element of order N, and ψ_k are the interpolation polynomials evaluated at point k. The basis functions ψ_k are constructed as the tensor product of the one-dimensional functions $h_p(\xi(\mathbf{x}))$, $h_q(\eta(\mathbf{x}))$, and $h_l(\zeta(\mathbf{x}))$ as:

$$\psi_k = h_p(\xi(\mathbf{x})) \otimes h_q(\eta(\mathbf{x})) \otimes h_l(\zeta(\mathbf{x})),$$

$\forall p, q, l = 0, ..., N$. $h_p(\xi(\mathbf{x}))$, $h_q(\eta(\mathbf{x}))$, and $h_l(\zeta(\mathbf{x}))$ are the basis functions associated with the N LGL points ξ_p, η_q, and ζ_l respectively, given by the roots of

$$(1-\xi^2)P_N^{'}(\xi) = 0,$$

where $P_N'(\xi)$ is the derivative of the N^{th}-order Legendre polynomial. Given these definitions, the one-dimensional Lagrange polynomials $h_p(\xi)$ are

$$h_p(\xi) = -\frac{1}{N(N+1)}\frac{(1-\xi^2)P_N'(\xi)}{(\xi-\xi_p)P_N(\xi_p)}.$$

The functions $h_q(\eta), h_l(\zeta)$ are computed in the same way. The same expansion (11) is used to construct the time and space derivatives of q_N. We write:

$$\begin{aligned}
\frac{\partial q_N(\mathbf{x},t)}{\partial t}|_{\Omega_e} &= \sum_{k=1}^{(N+1)^3} \psi_k(\mathcal{F}_{\Omega_e}^{-1}(\mathbf{x}))\frac{\partial q_N(\mathbf{x}_k,t)}{\partial t}, \\
\frac{\partial q_N(\mathbf{x},t)}{\partial \mathbf{x}}|_{\Omega_e} &= \sum_{k=1}^{(N+1)^3} \frac{\partial \psi_k(\mathcal{F}_{\Omega_e}^{-1}(\mathbf{x}))}{\partial \mathbf{x}} q_N(\mathbf{x}_k,t).
\end{aligned} \tag{12}$$

The integrals are computed by numerical quadrature on the reference element as follows:

$$\int_{\Omega_e^h} \mathbf{q}(\mathbf{x},t)\mathrm{d}\mathbf{x} = \int_{\hat{\Omega}_e^h} \mathbf{q}(\xi,t)|\mathbf{J}(\xi)|\mathrm{d}\xi \approx \sum_{p,q,l=1}^{N_{lgl}} q(\xi_p,\eta_q,\zeta_l,t)|\mathbf{J}(\xi_p,\eta_q,\zeta_l)|\omega_p^\xi\omega_q^\eta\omega_l^\zeta, \tag{13}$$

where the Gaussian quadrature weights $\omega_{p,q,l}$ are computed as

$$\omega_{p,q,l} = \frac{2}{N(N+1)}\left(\frac{1}{P_N(\xi_p,\eta_q,\zeta_l)}\right)^2.$$

The substitution of the expansions (11,12) into the weak form (10) yields the semi-discrete (in space) matrix problem

$$\frac{\partial \mathbf{q}}{\partial t} = \widehat{\mathbf{D}}^\mathcal{T}\mathbf{F}(\mathbf{q}) + \mathbf{S}(\mathbf{q}) \tag{14}$$

where, for the global mass and differentiation matrices, M and $\mathbf{D}$, we have that $\widehat{\mathbf{D}} = M^{-1}\mathbf{D}$. The global matrices are obtained from their local counterparts, M^e and $\mathbf{D}^e$, by means of the direct stiffness summation operation that maps the local degrees of freedom of an element Ω_e^h to the corresponding global degrees of freedom in Ω^h, and adds the element values in the global system. By construction, $\mathbf{M}$ is diagonal (assuming inexact integration), with an obvious advantage if explicit time integration is used.

3.2 Time discretization

The discretization in time is made by the Implicit-Explicit (IMEX) method of [6].

4 Numerical Tests

In the following section, the SEM-LES method presented in the previous Sections is tested against a suite of standard benchmarks of ubiquitous use when testing new atmospheric dynamical cores.

First, the model is verified in dry mode. We perturb a neutrally stable atmosphere with thermal anomalies that vary in definition and size. Because these tests do not have an analytic solution, the metrics that we use are based on comparison with the literature using the values of the extrema and the front velocity of the moving thermals. These tests include the rising thermal bubble in a large domain [1], and a modified density current [1, 24]. Once we have verified the ability of the model to handle dry dynamics on scales that are meaningful for atmospheric simulations, we solve a fully three-dimensional squall line (i.e. thermal convection with warm rain) triggered by a thermal perturbation of a realistic moist, partially unstable, background state.

Given that the analytical solution does not exist, it must be understood that these tests can only give a qualitative (and relative) information on the accuracy that one model can achieve.

4.1 Dry atmosphere

The background state is characterized by a neutral atmosphere with uniform potential temperature θ and with a background pressure p in hydrostatic equilibrium such that

$$p = p_0 \left(1 - \frac{g}{c_p \theta_0} z\right)^{c_p/R}, \tag{15}$$

where θ_0 is the potential temperature at the surface. The equation of state (2) is used to derive ρ:

$$\rho = \frac{p_0^{R/c_p}}{R\theta_0}\ p^{c_v/c_p}. \tag{16}$$

4.1.1 Case 1: Warm bubble in a large domain

The convection of a warm bubble in a uniform environment has been widely used by different authors (e.g. [21, 12, 1]) to test their codes. Similarly to [1] and [25], the domain extends within $[0, 10000] \times [-\infty, \infty] \times [0, 10000]\,\mathrm{m}^3$. In the y-direction the domain extends infinitely A large cylindrical bubble of $x-$ and $z-$ radii $r_0 = 2000\,\mathrm{m}$ is centered in $(x_c, z_c) = (10000, 2000)\,\mathrm{m}$ and is initially at rest. This warm region is used to perturb

the atmosphere that is initially at a uniform potential temperature $\theta = \theta_0 = 300$ K. The perturbation is given as a linear function of $R = \sqrt{(x - x_c)^2 + (z - z_c)^2}$ by

$$\theta' = \begin{cases} 0 & \text{if } R > r_0 \\ \\ A\,[1.0 - R/r_0] & \text{if } R \leq r_0, \end{cases} \tag{17}$$

where $A = 2.0$ K is the perturbation amplitude. The initial velocity field is zero everywhere. Periodic boundary conditions are used along y whereas no-flux conditions are set in x and z.

Results Case 1 The final time is set to $t_f = 1020\,s$. We perform three runs on four different resolutions: 1) $\overline{\Delta x} = \overline{\Delta z} = 12.5\,m$, 2) $\overline{\Delta x} = \overline{\Delta z} = 25\,m$, 3) $\overline{\Delta x} = \overline{\Delta z} = 50\,m$, and 3) $\overline{\Delta x} = \overline{\Delta z} = 100\,m$. The different resolutions were used to analyze the behavior of the method as the grid is refined, although no proper convergence study was made. Fig. 1 shows the values of the perturbation $\theta' = \theta - \theta_0$ for the four simulations. The results qualitatively agree with those of [1]. However, quantitatively we notice that the amount of diffusivity that is being added by the method seems to be just enough to stabilize the solution, with a limited amount of diffusion in the solution. This statement can be quantified by looking at the values of the extrema in Table 1. We notice that the value of the maxima and minima increase, in absolute value, as the grid is refined. A possible explanation can be searched in the fact that the stabilization method at hand is a function of the residual of the solution. As the grid is refined, the amount of artificial diffusion decreases proportionally to the square of the grid resolution. On a finer grid, less stabilization is necessary; as less diffusion is then added, the oscillatory behavior typical of high order spectral elements becomes more visible; although stabilization cannot be compromised by that.

Negative values of θ in Table 1 indicate the presence of local undershoots. In our case, a possible solution is the addition of a discontinuity capturing scheme to preserve monotonicity. In the current 3D code used for this study, we have not implemented the successful shock capturing method used for tracers in the atmosphere in [17]. This approach will be reported in a future article.

Remark: In Table 1, the results relative to the *Advanced Research Weather Research and Forecasting* modeling system (WRF-ARW) [22] were obtained by [1] using fifth- and third-order finite differences in the horizontal and vertical directions, respectively, and adding artificial viscosity with diffusivity coefficient $\mu = 15\,\mathrm{m}^2\,\mathrm{s}^{-1}$ to preserve stability. The run of the *f-wave* solver in the same reference employed a second-order finite volume scheme.

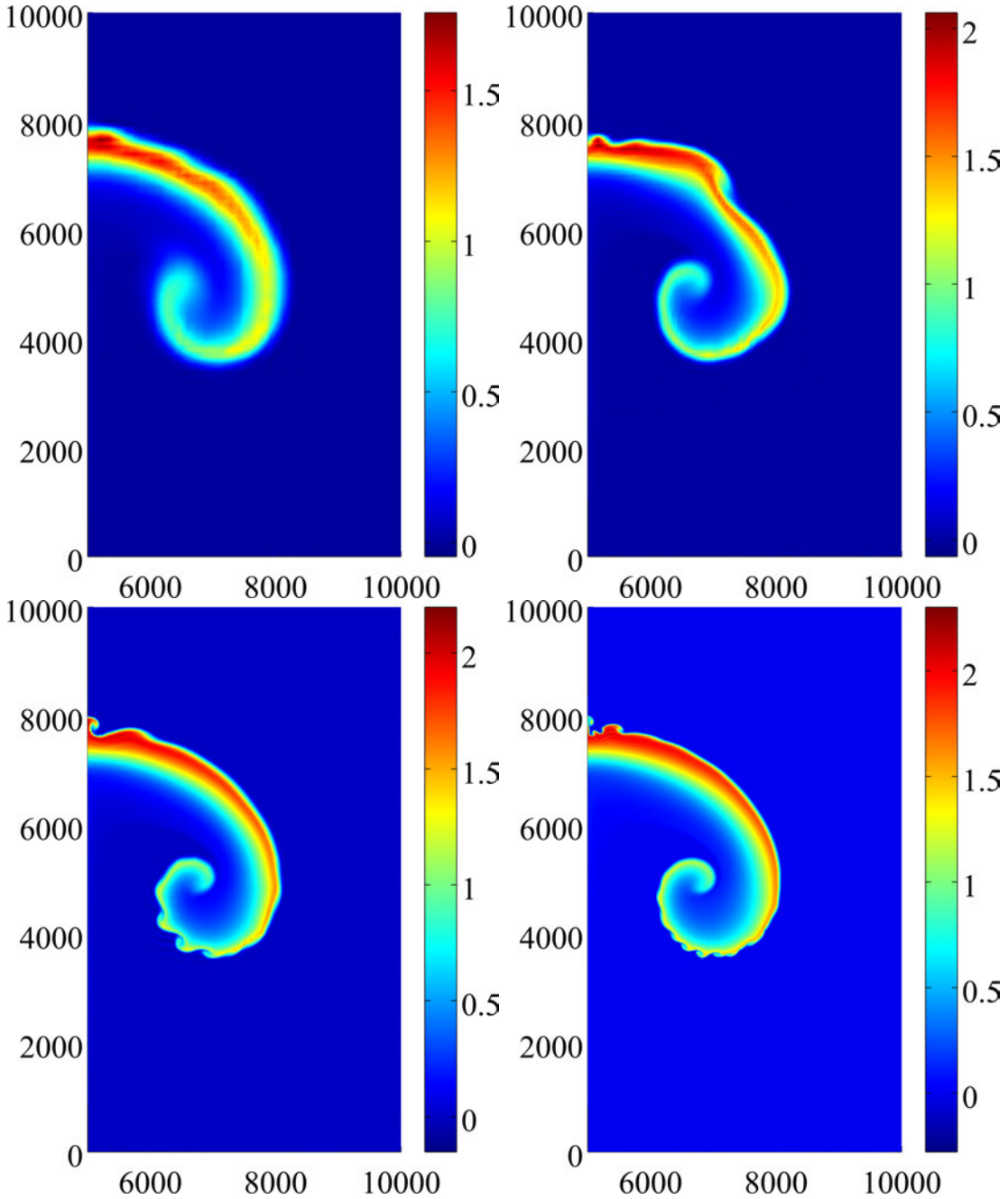

Figure 1: Case 1: θ' at $t = 1020$ s. Top left: $\overline{\Delta z} = \overline{\Delta x} = 100$m. Top-right: $\overline{\Delta z} = \overline{\Delta x} = 50$m. Bottom-left: $\overline{\Delta z} = \overline{\Delta x} = 25$m. Bottom-right: $\overline{\Delta z} = \overline{\Delta x} = 12.5$m.

4.1.2 Case 2: Density current

The density current was introduced in [5] and became a standard benchmark in the development of atmospheric codes [24]. Like in [1], in this paper the benchmark is slightly

Table 1: Case 1. Comparative results of $\theta'_{min,max}$ (K) and $(u,w)_{min,max}$ ($\mathrm{m\,s^{-1}}$) at 1020 s. LES (SEM), VMS (FE) at different resolutions, WRF-ARW (FD), and f-wave (FV) are compared. The results from WRF-ARW were found with an additional artificial diffusion with constant $\mu = 15\,\mathrm{m^2\,s^{-1}}$.

Model	$\mu = 15\,\mathrm{m^2\,s^{-1}}$	θ'_{min}	θ'_{max}	u_{min}	u_{max}	w_{min}	w_{max}
LES (12.5 m)	NO	-2.78e-1	2.30	-12.27	10.78	-11.22	14.50
LES (25 m)	NO	-1.53e-1	2.20	-11.72	10.73	-10.94	14.32
LES (50 m)	NO	6.61e-2	2.06	-9.98	9.81	-10.58	13.52
LES (100 m)	NO	-4.73e-2	1.76	-9.03	7.32	-9.07	12.44
VMS (50 m) [19]	NO	-1.38e-2	1.24	-10.21	10.21	-8.93	14.47
VMS (125 m) [19]	NO	-1.08e-2	1.01	-8.90	8.90	-7.43	14.03
VMS (250 m) [19]	NO	-1.53e-2	0.89	-7.18	7.18	-6.65	12.09
f-wave (125m) [1]	NO	-1.0e-2	1.39	-8.53	8.53	-7.75	13.95
WRF-ARW (125m) [1]	YES	-6.0e-2	1.65	-5.05	5.05	-5.0	11.5

modified and run without the constant and uniform artificial diffusion with coefficient $\mu = 75\,\mathrm{m^2\,s^{-1}}$. This is because we are interested in understanding the way the LES-like method described so far can serve as a stabilizing tool without the need for further viscosity. The initial base-state is at uniform potential temperature $\theta = \theta_0 = 300\mathrm{K}$ within the domain $[-25600, 25600] \times [-\infty, \infty] \times [0, 6400]\,\mathrm{m^3}$. A perturbation of θ centered in $(x_c, z_c) = (0, 3000)\,\mathrm{m}$ and with radii $(r_x, r_z) = (4000, 2000)\,\mathrm{m}$ is given by the function

$$\theta' = \begin{cases} 0 & \text{if } R > 1 \\ \\ A\left[\frac{1+\cos(\pi_c R)}{2}\right] & \text{if } R \leq 1 \end{cases} \tag{18}$$

where the perturbation amplitude is $A = -15$ K and $R = \sqrt{(x - x_c)/r_x^2 + (z - z_c)/r_z^2}$. Periodic boundary conditions are used along y whereas no-flux conditions are set in x and z. The initial velocity is zero.

Results case 2: Figs. 2 and 3 show the contours of $\theta' = \theta - \theta_0$ at $t_f = 600\,\mathrm{s}$ and $t_f = 900\,\mathrm{s}$ for three different resolutions: 1) $\Delta x = \Delta z = 100\,m$, 2) $\Delta x = \Delta z = 50\,m$, and 3) $\Delta x = \Delta z = 25\,m$. The cold perturbation introduces a heavier pool of air whose downward motion is responsible for the development of the propagating front. Inertia causes the top layers of the front to pull back and gives rise to Kelvin-Helmholtz structures.

Being inviscid, the results should compare with those in [1]. At comparable resolution, we observe the same rotating structures. To measure the front position at $t_f = 900\,\mathrm{s}$, we take the node on the ground where $\theta' = -1$ K. A comparison of the front position and $\theta'_{max,min}$ with respect to the referenced literature is reported in Table 2. As the resolution decreases, the front appears slower; this fact is also observed in Fig. 5 of [24].

As the resolution is increased, the amount of structures that are resolved increases as

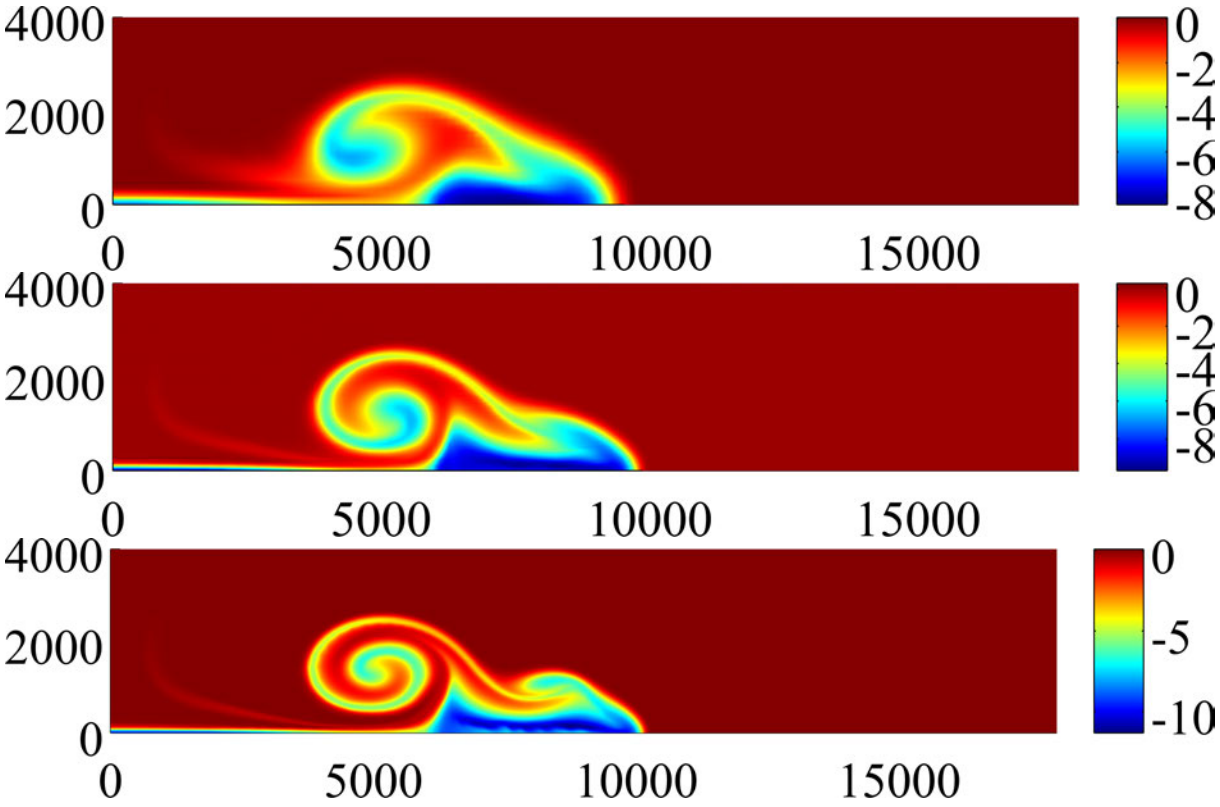

Figure 2: Density current: θ' at $t = 600$ s. From top to bottom: $\overline{\Delta z} = \overline{\Delta x} = 100$m, $\overline{\Delta z} = \overline{\Delta x} = 50$m, $\overline{\Delta z} = \overline{\Delta x} = 25$m.

well. Without the large viscosity that homogenizes the solution as done in [24] with the sole target of reaching convergence, the inviscid, non-linear, and non-steady solution that we present here is not expected to show signs of space-convergence. The same behavior was observed in [18], where VMS was used to stabilize a finite element discretization of the same model. We, rather, expect more and more structures to be resolved until the smallest refinement of the order of the subgrid scales is reached. The energy spectrum of this simulation is compared against the theoretical $-5/3$ Kolmogorov theory in Fig. 4.

4.2 Moist dynamics

We now assess the ability of LES-SEM to simulate moist dynamics in a realistic environment. The initial state for the simulation of the convective storm is defined by a real measurement of the thermodynamic and water quantities along a vertical column. The sounding data are plotted in Fig. 5. The lower troposphere is characterized by a layer of unsaturated water vapor (q_v) that decreases to zero with height. For the storm to initiate and develop, an unstable atmosphere is necessary in the lower troposphere. A typical condition in stormy weather is an unstable atmosphere below the tropopause above which

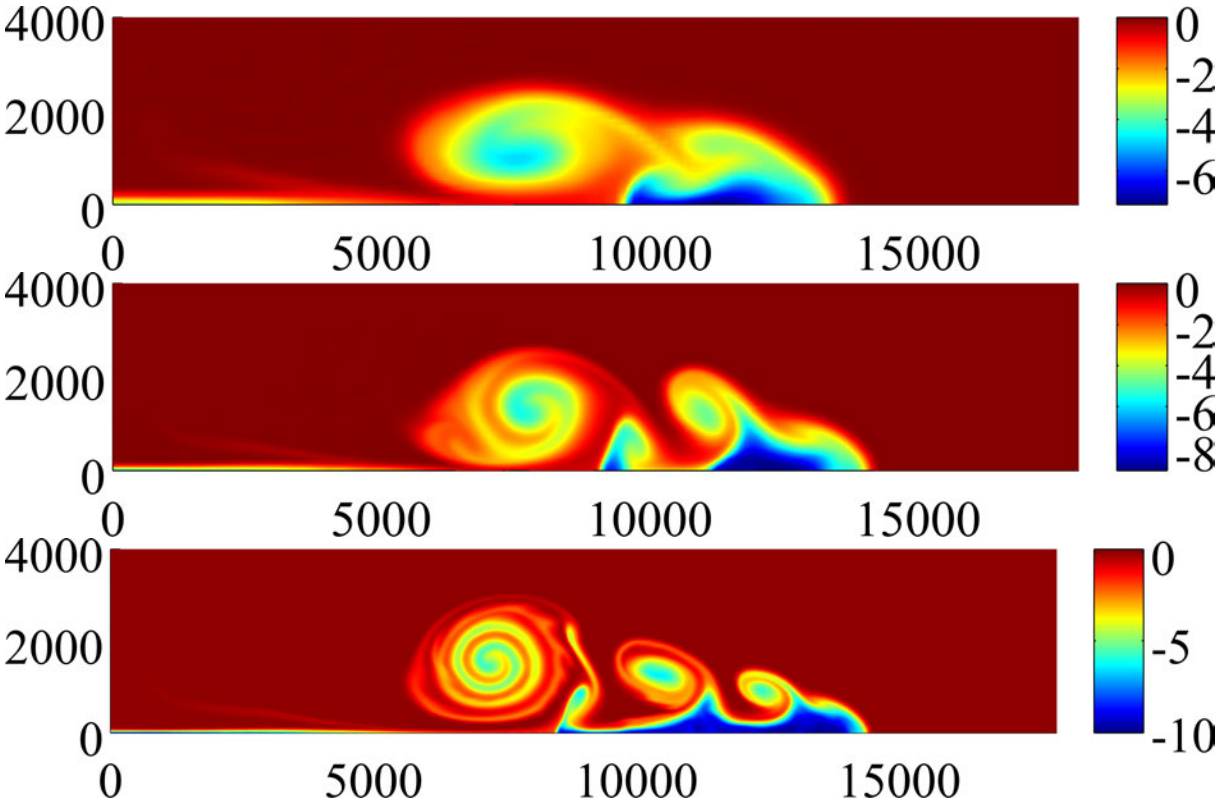

Figure 3: Density current: θ' at $t = 900$ s. From top to bottom: $\overline{\Delta z} = \overline{\Delta x} = 100$m, $\overline{\Delta z} = \overline{\Delta x} = 50$m, $\overline{\Delta z} = \overline{\Delta x} = 25$m.

a thermal inversion causes the stability to change. The formation of the storm is possible as long as the convective available potential temperature (CAPE) is above 2 kJ. Like the dry case, no analytic solution exists. Furthermore, the solution of moist convection is highly dependent on the resolution (see, e.g., [3, 4]) so that a convergence analysis is not an option to fully evaluate the model. Given the scope of this paper, we will limit ourselves to simulate a fully three-dimensional squall line at one suitable resolution with the sole intent of verifying that the code can handle realistic problems with moisture. A thorough analysis of moist convection using NUMA will be presented in a work that is being currently developed by the authors.

4.2.1 Case 3: 3D convective cell

The three-dimensional simulation of a convective cell is defined in the domain $[-80000, 80000] \times [-60000, 60000] \times [0, 24000]\,\mathrm{m}^3$. The initial field is perturbed by a temperature anomaly θ' 3 K warmer than the surrounding environment. The perturbation is centered in $(x_c, y_c, z_c) = (0, 0, 2000)$ m and is defined by

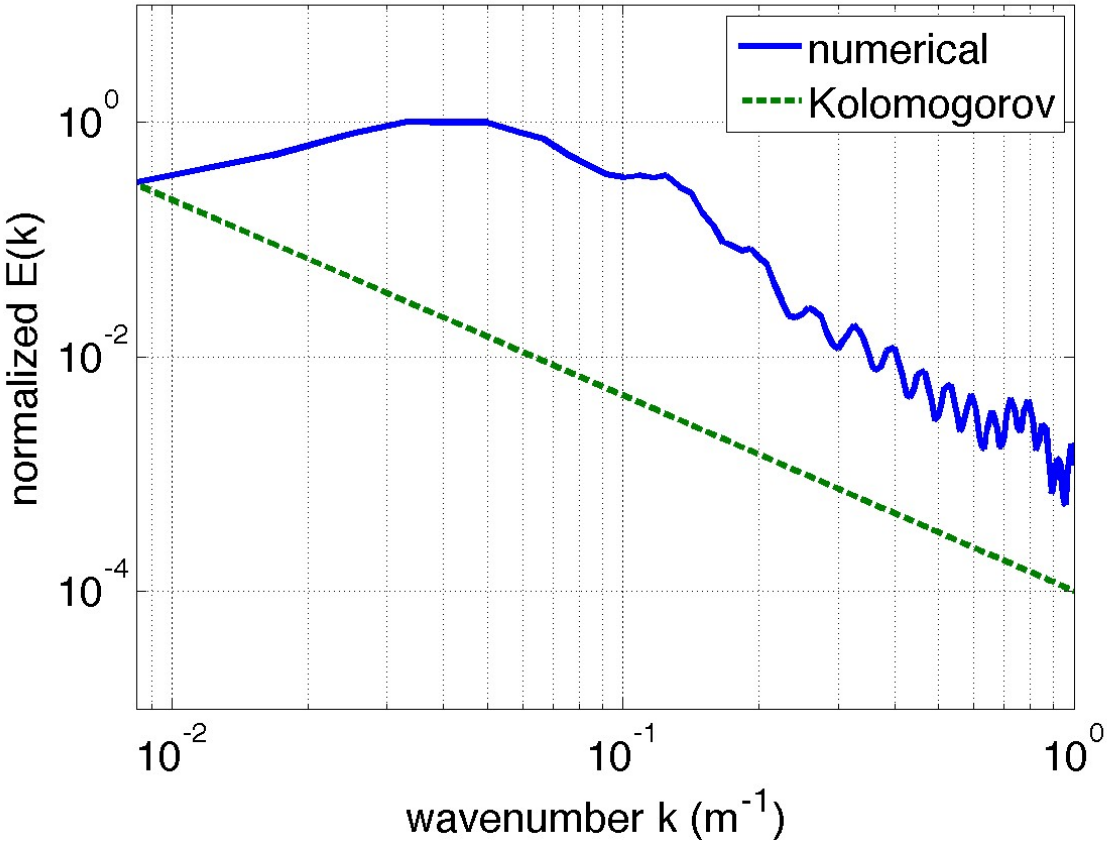

Figure 4: Density current: energy spectrum of the simulation with $\overline{\Delta x} = \overline{\Delta z} = 100\,m$.

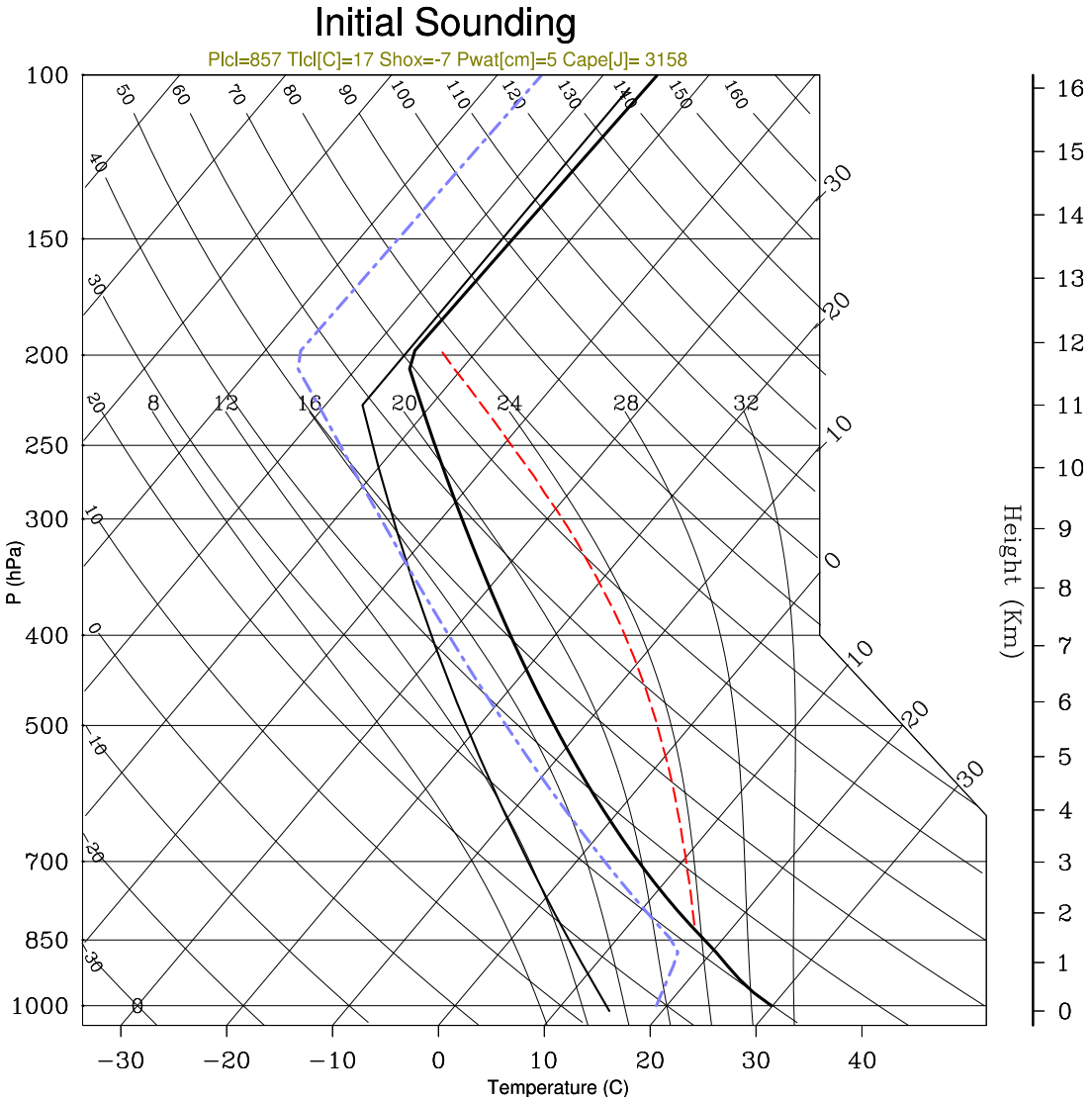

Figure 5: Skew-T plot of the initial sounding. The thick black continuous and the dash-dotted purple lines represent, respectively, temperature and the dew point temperature. The dashed red curve is the wet adiabatic curve. The area between the wet adiabatic and the T curve is equivalent to the value of convective available potential temperature.

Table 2: Case 3. Comparative results of $\theta'_{min,max}$ and front location at 900s. LES (SEM), VMS (FE), WRF-ARW V2.2 (FD), f-wave (FV), Spectral Elements (SE), filtered Discontinuous Galerkin (DG), REFC, REFQ and PPM results are compared. All models but LES-SEM and VMS used artificial diffusion with constant $\mu = 75\,\mathrm{m^2\,s^{-1}}$.

Model	$\mu = 75\,\mathrm{m^2\,s^{-1}}$	θ'_{min}	θ'_{max}	Front Location [m]
LES (25 m)	NO	-10.21	0.17	14440
LES (50 m)	NO	-9.12	0.03	14166
LES (100 m)	NO	-7.340	0.02	13550
VMS [19] (25 m)	NO	-13.98	7.81	14890
VMS [19] (50 m)	NO	-12.91	3.54	14629
VMS [19] (75 m)	NO	-10.23	2.55	14487
VMS [19] (100 m)	NO	-8.0	2.03	14355
WRF-ARW 50 m	YES	-7.32	0.0	14470
SE [7] 50m	YES	-8.90	1.2e-4	14767
DG [7] 50m	YES	-8.90	1.2e-4	14767
f-wave (FV) [1] 50 m	YES	-9.82	8.92E-03	14975
REFC [24] 50 m	YES	-9.77	0.0	14437
REFQ [24] 50 m	YES	-10.00	0.0	14409
PPM [24] 50 m	YES	-8.31	0.022	15027

$$\theta' = \theta_c\, cos^2 \frac{\pi R}{2} \qquad \text{if } R \leq 1, \tag{19}$$

where

$$R = \sqrt{(x - x_c)/r_x^2 + (y - y_c)/r_y^2 + (z - z_c)/r_z^2},$$

and $(x_r, y_r, z_r) = (10000, 10000, 1500)\,\mathrm{m}$.

Results Case 3. Ω^h is subdivided into $40 \times 30 \times 24$ elements of order 4. A stretched grid along z is used to make the resolution higher in the lower atmosphere. The horizontal resolution is equal to $\overline{\Delta x} = \overline{\Delta y} = 1000\,\mathrm{m}$. $\overline{\Delta z}$ varies from 200 m in the lowest layer to 525 m in the upper atmosphere. The domain is crossed by a horizontal wind along the x-direction. The velocity decreases linearly from $12\,m\,s^{-1}$ on the ground to $0\,\mathrm{m\,s^{-1}}$ at $z = 2000\,\mathrm{m}$. A no-slip condition is applied on the surface boundary while periodic boundaries are defined along x and y. A Rayleigh type absorbing layer is included at $z \geq 19000\,\mathrm{m}$.

The first cloud forms at approximately 900 s. The presence of the wind shear immediately breaks the axial symmetry of the cloud and allows the storm to self-sustain as long as there is a flow of water vapor to feed the core of the storm. The first condensation of q_c into q_r occurs at approximately 1200 s and the first rain reaches the ground about 600 s later. As convection reaches the tropopause, the mean vertical motion of the cloud

stops due to the higher stability of the environment. A realistic rendering of the storm at $t = 9000\,\mathrm{s}$ is shown in Fig. 6. The view of the simulated cloud is from the ground using a realistic perspective; the camera is centered at $(x, y, z)_{camera} = (48, 41, 0)$ km, with focal points at $(x, y, z)_{focal,point} = (4.4, 0, 13.3)$ km. A qualitative representation of the fully developed storm at the same time is plotted in Figs. 7 and 8. The quantitative values of q_c and q_r are plotted in Fig. 9. The values are qualitatively and quantitatively comparable to the literature. For a direct comparison of a single cell convective storm, please, see Chapter 6 of [16], where this specific test case was defined and executed using a stabilized finite element method.

Figure 6: 3D Squall Line: camera view from $(x, y, z)_{camera} = (48, 41, 0)$ km, with focal points at $(x, y, z)_{focalpoint} = (4.4, 0, 13.3)$ km. The rain is visible from the vertical streaks illuminated by the sun. Rendering using MAYA.

5 Conclusions

We extended to high order spectral elements the LES-based stabilization method first introduced in [20] for the finite element solution of fully compressible flows. We explored the capabilities of this inexpensive technique to solve the Euler equations of stratified flows at the low-Mach regimes encountered in atmospheric flows. When applied to dry and moist simulations, the current implementation appears to give satisfactory results that are comparable to others presented in the literature. Without the need for any additional viscosity, this dynamic LES scheme proved to be sufficient to stabilize the

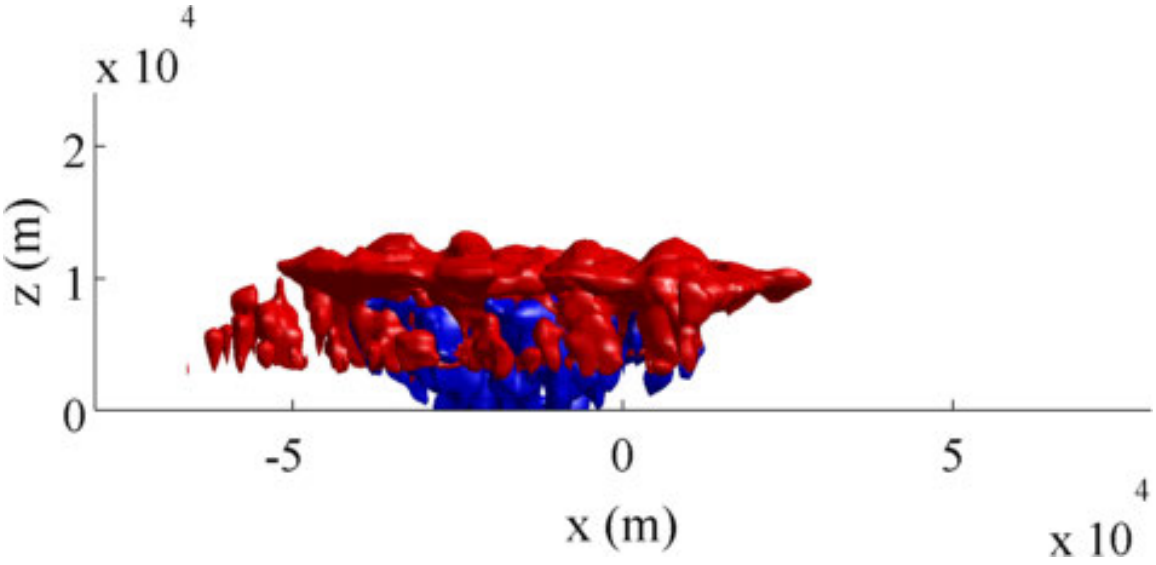

(a) View from 0° in azimuth and 0° in elevation.

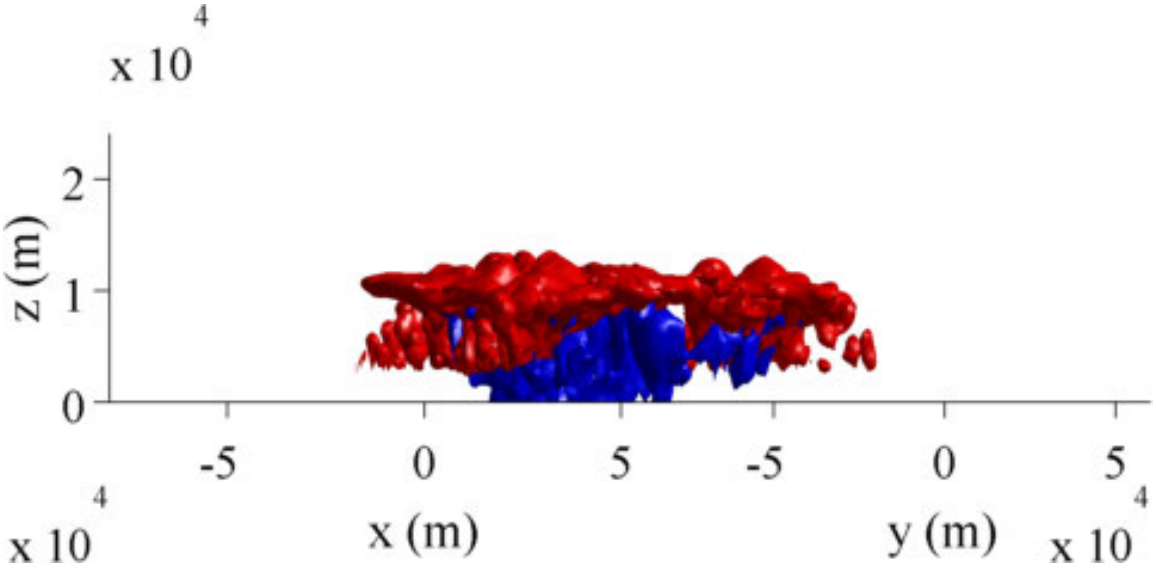

(b) View from 45° in azimuth and 0° in elevation.

Figure 7: 3D Squall Line: $\overline{\Delta x} = \overline{\Delta y} = 1000\,m$ $\overline{\Delta z} = 245\,m$ ($40 \times 30 \times 24$ elements of order 4). Isosurface of q_c (red) and q_r (blue) at $t_f = 9000\,s$.

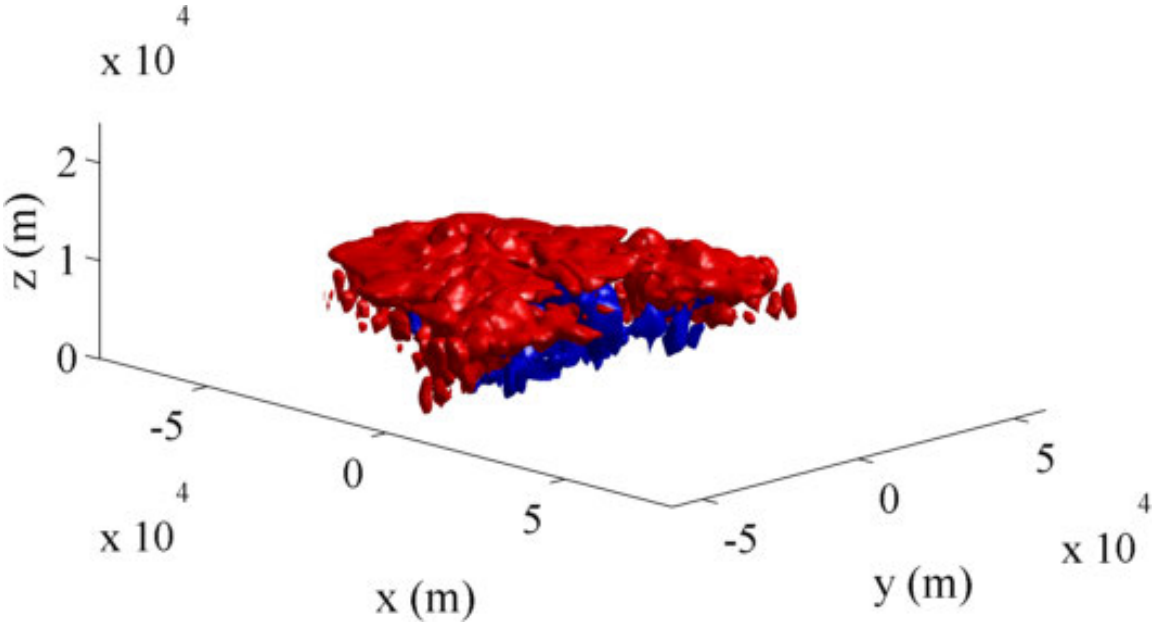

(a) View from 45° in azimuth and 15° in elevation.

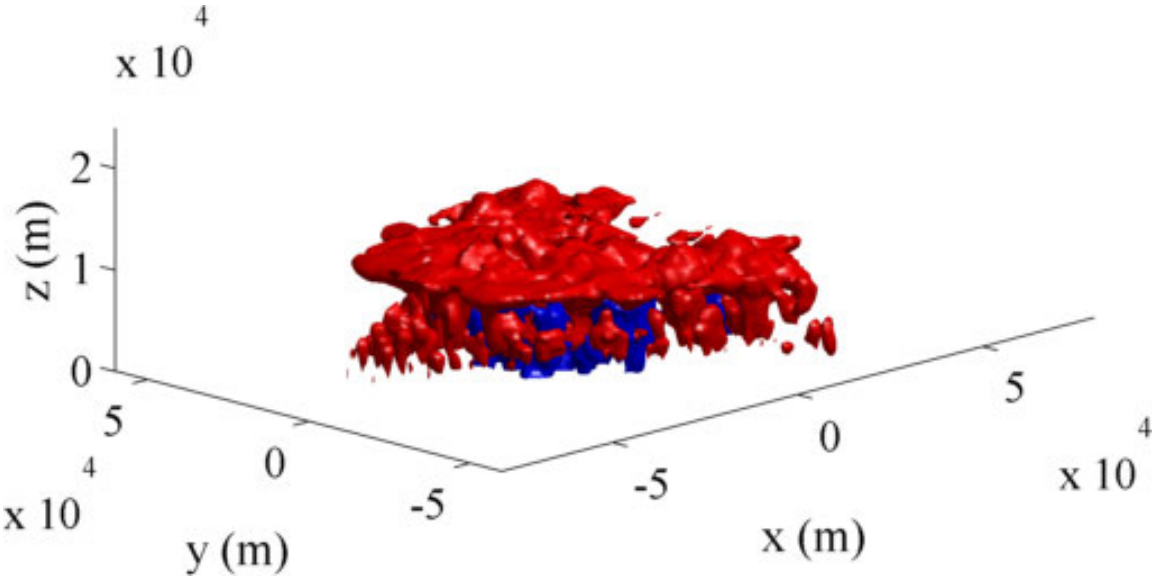

(b) View from −45° in azimuth and 15° in elevation.

Figure 8: As Figure 7, but from a different perspective.

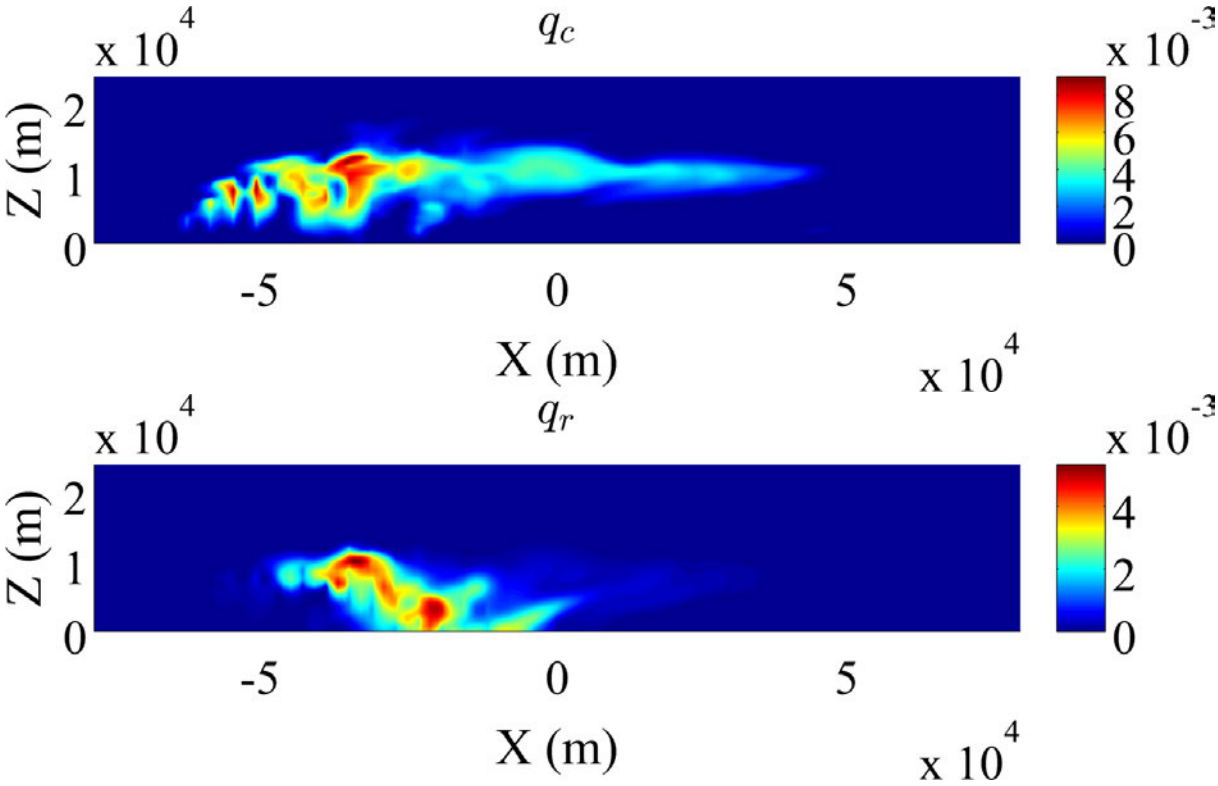

Figure 9: 3D Squall Line: vertical slice of q_c (top) and q_r (bottom) at $y = 0.0\,m$. $t_f = 9000\,s$. The quantities are measured in kg/kg.

spectral element solution of the Euler equations in atmospheric applications. However, since a thorough analysis was not carried out to evaluate this approach in terms of its turbulence modeling properties, much additional work is necessary to fully assess it in its applicability as a turbulence closure for atmospheric simulations.

6 Acknowledgements

The authors gratefully acknowledge the support of the Office of Naval Research through program element PE-0602435N, the National Science Foundation (Division of Mathematical Sciences) through program element 121670, and the Air Force Office of Scientific Research through the Computational Mathematics program. The work of the first author was supported by the National Academies through a National Research Council fellowship. The authors would like to thank Dr. Murtazo Nazarov (Texas A&M) for useful comments on the methodology. They also thank Dr. James F. Kelly (Exa Corp., Burlington, MA) for providing the routines to compute the energy spectrum. All the plots were created with MATLAB. The commercial software MAYA was used for the cloud rendering.

REFERENCES

[1] N. Ahmad and J. Lindeman. Euler solutions using flux-based wave decomposition. *Int. J. Numer. Meth. Fluids*, 54:47–72, 2007.

[2] A N Brooks and T J R Hughes. Streamline upwind/Petrov-Galerkin formulations for convective dominated flows with particular emphasis on the incompressible navier-stokes equations. *Comput. Methods Appl. Mech. Eng.*, 32:199–259, 1982.

[3] G H. Bryan and H. Morrison. Sensitivity of a simulated squall line to horizontal resolution and parameterization of microphysics. *Mon. Wea. Rev.*, 140:202–225, 2011.

[4] J. C. Bryan, G. H. Wyngaard and J. M. Fritsch. Resolution requirements for the simulation of deep moist convection. *Mon. Wea. Rev.*, 31:2394, 2003.

[5] R. Carpenter, K. Droegemeier, P. Woodward, and C. Hane. Application of the piecewise parabolic method (PPM) to meteorological modeling. *Mon. Wea. Rev.*, 118:586–612, 1990.

[6] F X. Giraldo, J F.. Kelly, and E. Constantinescu. Implicit-explicit formulations of a three-dimensional Nonhydrostatic unified model of the atmosphere (NUMA). *SIAM J. Sci. Comput.*, 35, 2013.

[7] F. X. Giraldo and M. Restelli. A study of spectral element and discontinuous Galerkin methods for the Navier-Stokes equations in nonhydrostatic mesoscale atmospheric modeling: Equation sets and test cases. *J. Comput. Phys.*, 227:3849–3877, 2008.

[8] G. Houzeaux and J. Principe. A variational subgrid scale model for transient incompressible flows. *International Journal of Computational Fluid Dynamics*, 22:135–152, 2008.

[9] T. Hughes. Multiscale phenomena: Green's functions, the Dirichlet-to-Neumann formulation, subgrid scale models, bubbles and the origins of stabilized methods. *Comput. Methods Appl. Mech. and Engrg.*, 127:387–401, 1995.

[10] T J R Hughes, L P Franca, and G M Hulbert. A new finite element formulation for computational fluid dynamics: III. the Galerkin/least-squares method for advection-diffusive equations. *Comput. Methods Appl. Mech. Eng.*, 73:329–336, 1989.

[11] C. Jablonowsky and D L. Williamson. The pros and cons of diffusion, filters and fixers in atmospheric general circulation models. In P H. Lauritzen, C. Jablonowski, M A. Taylor, and R D. Nair, editors, *Numerical Techniques for Global Atmospheric Models*, volume 80 of *Lecture notes in computational science and engineering*, pages 381–482. Springer, 2011.

[12] Z. Janjic, J. Gerrity, and S. Nickovic. An alternative approach to non-hydrostatic modeling. *Mon. Wea. Rev.*, 129:1164–1178, 2001.

[13] J. F. Kelly and F. X. Giraldo. Continuous and discontinuous Galerkin methods for a scalable three-dimensional nonhydrostatic atmospheric model: Limited-area mode. *J. Comput. Phys.*, 231:7988–8008, 2012.

[14] E. Kessler. On the distribution and continuity of water substance in atmospheric circulation. *Meteorol. Monogr.*, 10:32, 1969.

[15] J. Klemp and R. Wilhelmson. The simulation of three-dimensional convective storm dynamics. *J. Atmos. Sci.*, 35:1070–1096, 1978.

[16] S. Marras. *Variational Multiscale Stabilization of Finite and Spectral Elements for Dry and Moist Atmospheric Problems*. PhD thesis, Universitat Politécnica de Catalunya, 2012.

[17] S. Marras, J. F. Kelly, F. X. Giraldo, and M. Vázquez. Variational multiscale stabilization of high-order spectral elements for the advection-diffusion equation. *J. Comput. Phys.*, 231:7187–7213, 2012.

[18] S. Marras, M. Moragues, M R. Vázquez, O. Jorba, and G. Houzaux. Simulations of moist convection by a variational multiscale stabilized finite element method. *J. Comput. Phys.*, 252:195–218, 2013.

[19] S. Marras, M. Moragues, M R. Vázquez, O. Jorba, and G. Houzaux. A variational multiscale stabilized finite element method for the solution of the Euler equations of nonhydrostatic stratified flows. *J. Comput. Phys.*, 236:380–407, 2013.

[20] M. Nazarov and J. Hoffman. Residual-based artificial viscosity for simulation of turbulent compressible flow using adaptive finite element methods. *Int. J. Numer. Methods Fluids*, 71:339–357, 2013.

[21] A. Robert. Bubble convection experiments with a semi-implicit formulation of the euler equations. *J. Atmos. Sci.*, 50:1865–1873, 1993.

[22] W. Skamarock, J. Klemp, J. Dudhia, D. Gill, D. Barker, W. Wang, and J. Powers. A description of the Advanced Research WRF Version 2. Technical Report 468, NCAR TN STR, 2007.

[23] S. Soong and Y. Ogura. A comparison between axisymmetric abd slab0symmetric cumulus cloud models. *J. Atmos. Sci.*, 30:879–893, 1973.

[24] J. Straka, R. Wilhelmson, L. Wicker, J. Anderson, and K. Droegemeier. Numerical solution of a nonlinear density current: a benchmark solution and comparisons. *Int. J. Num. Meth. in Fluids*, 17:1–22, 1993.

[25] L. Wicker and W. Skamarock. A time-splitting scheme for the elastic equations incorporating second-order runge-kutta time differencing. *Mon. Wea. Rev.*, 126:1992–1999, 1998.